von Karman Institute for Fluid Dynamics

Lecture Series 2025-01

MEASUREMENT, MODELLING AND SIMULATIONS TECHNIQUES FOR NOVEL AIRCRAFT ARCHITECTURES

November 4-6, 2024

SCALE-RESOLVED AEROACOUSTIC APPROACHES: HYBRID RANS/LES AND WALL-MODELED SIMULATIONS

M. Terracol
ONERA, DAAA, Institut Polytechnique de Paris, France

1 Introduction

Reducing aircraft noise has become a priority for manufacturers, driven by the continuous rise in air traffic and increasingly stringent noise regulations. Among the list of the different contributors to aircraft noise, airframe noise is a significant factor, especially during approach and landing phases. One can site for instance the noise generated by the flow around the landing gears or around the high-lift devices, such as slats and flaps, which are deployed to enhance lift at low speeds. To further reduce noise and pollutant emissions, new aircraft designs are being explored, including advanced propulsion systems like Distributed Electric Propulsion (DEP) and Boundary Layer Ingestion (BLI). These innovative concepts introduce unconventional physical mechanisms that necessitate thorough investigation and understanding. For that reason, it is of outstanding importance to develop numerical and experimental approaches capable of not only predicting the noise generated by such designs but also of understanding the main involved physical phenomena responsible for noise generation, in order to propose active or passive noise control solutions. Modern aeroacoustic studies use Computational AeroAcoustics (CAA) hybrid techniques to predict noise generation and propagation across a wide frequency range. The first step of these approaches is to get an accurate prediction of the unsteady turbulent flows linked to noise sources generation.

It is worth noting that a large variety of noise sources is due to the presence of massively separated flow regions, interacting with solid boundaries. However, a proper resolution of such separated flows requires accurate predictions of the turbulent boundary layers developing around the different components. Indeed, improper predictions of the turbulent boundary layer properties may lead in practice to an erroneous location of separation and, as a consequence, to incorrect overall flow prediction. This can have a dramatic impact on the prediction of the overall acoustic field. Moreover, in some cases, the turbulent boundary layer may also interact directly with immersed components, such as in the case of BLI. As a consequence, predicting accurately its dynamics is even more important.

These lecture notes will provide a non-exhaustive presentation of several numerical approaches under consideration at ONERA that allow accurate aeroacoustic predictions of turbulent flows governed by turbulent boundary layer dynamics, over a range of Reynolds numbers characteristic of the aerospace and aeronautical industry ($10^6 \leq Re \leq 10^8$). Most of these approaches are based on hybrid RANS/LES methods and/or wall modeled approaches.

2 Motivations for hybrid RANS/LES and Wall-modeled approaches

When dealing with a scale-resolving numerical simulation of a turbulent flow, two main classes of method are generally possible:

- The Direct Numerical Simulation (DNS) approach, which aims at accounting for all the characteristic turbulent structures present in the flow, ranging from the largest energy-containing scales to the smallest eddies that resist to viscous dissipation *i.e.* KolmogorovâĂŹs length. For realistic values of the Reynolds number, the ratio between the sizes of the largest and smallest eddies is very large.

- The Large-Eddy Simulation (LES) approach, which relies on a scale separation between the largest scales of the flow including the main driving physical mechanisms and the small ones which are only responsible for a drain of energy. This approach proposes to resolve only the large-scale part while accounting for the small scales using a mathematical model. This technique reduces significantly the cost of the simulations compared to DNS for free shear flows, but remains a very CPU-consuming approach when the flow is in the presence of solid boundaries.

For LES, it can be shown that a large fraction of the computational cost is due to the resolution of the inner part of the boundary layer. This gave rise to the development of Wall-Modeled LES (WMLES) approaches, in which the idea is to resolve explicitly the turbulent fluctuations only in the outer part of the boundary layer, while using a so-called wall model in the inner part to model the turbulence effect on the mean flow quantities.

Several works (*e.g.* [12, 14, 20, 67]) have focused on the derivation of CPU cost estimates for these three respective approaches (DNS, LES and WMLES). We report here the estimates proposed by Deck *et al.*[20], inspired by the works by Choi and Moin [14]. Similar estimates have also been reported by Yang and Griffin [67]. These estimates are based on the general idea that one may consider n_x, n_y, n_z points per wavelength $\lambda_x, \lambda_y, \lambda_z$ in the respective x, y and z directions, with x the streamwise coordinate, y the wall-normal one and z refers to the span.
For a fully-developed[1] zero-pressure gradient turbulent boundary layer over a flat plate, between $x = x_0$ and $x = L_x$, on a span L_z, the overall number of grid points required to simulate the boundary layer thickness δ is expressed as:

$$N_{xyz} = \int_0^{L_z} \int_0^{\delta} \int_{x_0}^{L_x} \frac{n_x}{\lambda_x} \frac{n_y}{\lambda_y} \frac{n_z}{\lambda_z} \, dx \, dy \, dz \tag{1}$$

The integral in the wall-normal direction y can be split into two flow regions, the viscous sub-layer $0 < y < y_{vsl}$ and the region $y_{vsl} < y < \delta$ where turbulent effects dominate the viscous ones. Depending on the authors, the height of this sub-layer expressed in wall units y^+_{vsl} has typical values of 10 [20], 30 [67] and 100 [14].

Depending on the resolution approach, the characteristic lengthscales of interest (λ_x, λ_y, λ_z) differ significantly. For the DNS approach, they are proportional to the Kolmogorov scale η, *i.e.* the size of the smallest eddies. For the LES approach, they are proportional to the size of the largest energy-carrying eddies. These eddies are known to scale as function of the viscous length ν/u_τ in the viscous sub-layer and then as the local height y up to the boundary layer thickness δ. For the WMLES approach, the viscous sub-layer is modeled, while only the structures with a size proportional to the boundary layer thickness δ are resolved.

Therefore, the evaluation of the integral (1) requires local estimates of the boundary layer parameters, such as its thickness δ and the skin friction velocity u_τ. Using a classical seventh-power velocity assumption (e.g. [48]), the following correlations are considered for

[1]We only consider the fully-developed portion of the boundary layer, past a streamwise coordinate x_0. The cost associated to the development of the laminar and transitional boundary layer upstream of x_0 is omitted in these estimates, but may in some cases significantly increase the overall cost of the simulation.

the local boundary layer thickness δ, friction coefficient $C_f = \dfrac{\tau_w}{\frac{1}{2}\rho_\infty U_\infty^2}$ and skin friction velocity u_τ as functions of the local streamwise Reynolds number $Re_x = U_\infty x/\nu$:

$$\delta = 0.16\, x\, Re_x^{-\frac{1}{7}} \tag{2}$$

$$C_f = 0.027\, Re_x^{-\frac{1}{7}} \tag{3}$$

$$u_\tau = 0.116\, U_\infty\, Re_x^{-\frac{2}{7}} \tag{4}$$

Additionally, the Kolmogorov scale in the boundary layer is expressed as [20, 67]:

$$\eta = \nu/u_\tau \quad , \quad 0 < y < y_{vsl} \tag{5}$$

$$\eta = \kappa^{\frac{1}{4}}\, (\nu/u_\tau)^{-\frac{3}{4}}\, y^{\frac{1}{4}} \quad , \quad y_{vsl} \leq y < \delta \tag{6}$$

Using these different characteristic lengths in the integral (1) leads to several estimates for the required number of grid points as function of the targeted Reynolds number Re_{L_x}.

On the basis of these characteristic scales estimates, Yang and Griffin [67] also provide estimates for the number of time steps N_t required for reaching converged statistics, instead of the rough estimate $N_t \simeq N_{xyz}^{\frac{1}{3}}$ proposed by Reynolds [45].

Method	$\lambda_x, \lambda_y, \lambda_z$ $0 < y < y_{vsl}$	N_{xyz} $0 < y < y_{vsl}$	$\lambda_x, \lambda_y, \lambda_z$ $y_{vsl} < y < \delta$	N_{xyz} $y_{vsl} < y < \delta$	N_t	Overall cost $N_{xyz} \times N_t$
DNS	$C_x\eta$ $C_y\eta$ $C_z\eta$	$\propto Re_{L_x}^{13/7}$	$C_x\eta$ $C_y\eta$ $C_z\eta$	$\propto Re_{L_x}^{115/56}$	$\propto Re_{L_x}^{6/7}$	$\propto Re_{L_x}^{2.91}$
LES	$\Delta x_w^+\nu/u_\tau$ $C_y y_{vsl}^+\nu/u_\tau$ $\Delta z_w^+\nu/u_\tau$	$\propto Re_{L_x}^{13/7}$	$C_x y$ $C_y y$ $C_z y$	$\propto Re_{L_x}^{13/7}$	$\propto Re_{L_x}^{6/7}$	$\propto Re_{L_x}^{2.71}$
WMLES	Modeled	Modeled	$C_x\delta$ $C_y\delta$ $C_z\delta$	$\propto Re_{L_x}$	$\propto Re_{L_x}^{1/7}$	$\propto Re_{L_x}^{1.14}$

Table 1: Characteristic scales of interest and cost estimates for the different scale-resolving approaches. C_x, C_y and C_z denote proportionality constants. For the LES approach, Δx_w^+ and Δz_w^+ denote streamwise and spanwise targeted grid spacings, required for an appropriate representation of the near-wall streaky structures, while y_{vsl}^+ denotes to the viscous sub-layer height expressed in wall units.

Table 1 summarizes the characteristic lengthscales and obtained CPU cost scaling for the different resolution approaches. It is worth noting that the trends for DNS and LES are quite close[2], due to the high cost linked to the resolution of the viscous sub-layer

[2]However, it is worth remembering that even if the CPU costs associated to LES and DNS approaches share the same scaling in the viscous sub-layer, the proportionality constants may significantly differ as the acceptable near-wall grid resolutions expressed in wall units are usually larger for the LES approach.

in both cases. For instance, a typical increase of the Reynolds number by one order of magnitude results in an overall cost increase by factors of about 800 for DNS and 500 for LES, which rapidly yields to strong practical limitations.

Since the turbulent fluctuations in the viscous sub-layer are not directly resolved in the WMLES approach, the CPU cost associated to this approach is much lower than the DNS and LES, with a scaling with the Reynolds number of about $Re_{L_x}^{1.14}$. Therefore, this makes this approach very attractive for the numerical simulation of high-Reynolds-number wall-bounded flows.

Another alternative to keep the numerical simulation of wall-bounded flows at an acceptable cost rely on the use of hybrid RANS/LES approaches, where the general idea is to get rid of the explicit resolution of the near-wall turbulent fluctuations by focusing the computational effort only in specific physical regions of interest *e.g.* linked to the noise generation mechanisms in aeroacoustics. This is done in practice by adopting a RANS resolution of the attached boundary layers and switch to LES only in detached flow regions, where an explicit resolution of the shear layer dynamics is performed. Some of these so-called hybrid RANS/LES approaches, currently used and under development at ONERA, will be presented in the next section.

3 Hybrid RANS/LES approaches

As seen in the previous section, Large Eddy Simulations of wall bounded flows still suffer from strong practical limitations due to their high computational cost when the near-wall structures are directly resolved. For that reason, several hybrid methods which combine the RANS and LES techniques have been developed over the years to be able to deal with the unsteady simulation of realistic turbulent wall-bounded flows. The general common idea shared by all these different techniques is to rely on either a RANS resolution or a LES one, depending on the considered flow region. All these methods are more or less pertinent depending on the class of flow of interest. They can be recast as two main classes of hybrid methods, namely global and zonal methods. For a detailed discussion and presentation of these various techniques, the reader can refer to the book by Sagaut *et al.*[46] where an exhaustive review of such hybrid RANS/LES approaches is performed.

Today's most commonly used hybrid RANS/LES strategies are generally based on the Detached Eddy Simulation (DES) concept, originally developed by Spalart *et al.*[49] and for which several improvements have been proposed. This modeling strategy aims at taking benefit of the good performance and affordable computational cost of the RANS approach in attached boundary layers, while switching continuously to an LES-like method in massively separated areas "detached" from the wall, using a unique system of equations. This idea was first proposed in 1997 by Spalart *et al.*who introduced a simple modification in the Spalart-Allmaras RANS model [51]. The general simple idea to modify a RANS method into its hybrid RANS/LES formulation relies on an *ad-hoc* modification of its characteristic lengthscale L_{RANS} which is replaced by a new hybrid lengthscale. The most general expression for the hybrid lenghtscale is:

$$L_{hybrid} = L_{RANS} - f_P \max\left(0, L_{RANS} - L_{LES}\right) \tag{7}$$

where $f_P \in [0;1]$ is the so-called shielding function, aimed at providing a full shielding of the attached boundary layer in RANS mode ($f_P = 0$), while switching continuously to

the LES mode in separated areas ($f_P = 1$ and $L_{LES} \ll L_{RANS}$). The LES characteristic cutoff scale is expressed as $L_{LES} = C_{DES}\Delta$, with $C_{DES} = 0.65$ a modeling parameter. Depending on the specific hybrid method, the scale Δ may take different expressions.

In the following, we will focus on the specific case of the SA turbulence model [51] used as the underlying RANS method. In this case, the characteristic lengthscale is $L_{RANS} = d_w$ where d_w is the distance to the closest wall. However, it is worth noting that several other choices are possible, such as $L_{RANS} = \sqrt{k}/\omega$ when the $k-\omega$ model is considered as the underlynig RANS model, *e.g.* [53].

Original DES97 formulation
In the original formulation of the Detached-Eddy Simulation proposed by Spalart *et al.*[49] in 1997, the hybrid lengthscale is simply expressed as:

$$L_{DES} = \min\left(d_w, C_{DES}\Delta\right) \tag{8}$$

which corresponds to $f_P = 1$ and $L_{RANS} = d_w$ in the general expression (7).
The cutoff lengthscale Δ is taken as the largest dimension of the local grid cell:

$$\Delta = \max\left(\Delta x, \Delta y, \Delta z\right) \tag{9}$$

where Δx, Δy and Δz denote the local spatial grid resolution, in the respective streamwise, wall-normal and spanwise directions. According to this definition, the switch location is only governed by the grid resolution. Unfortunately, this leads in practice to several shortcomings when the grid is refined, since in this case, the switch from RANS to LES may occur inside the boundary layer and even close to the wall. In such a case, a so-called *Modeled Stress Depletion* may occur, which is characterized by a strong decay of the eddy viscosity, with no proper regeneration of resolved turbulent fluctuations. In the presence of an adverse pressure gradient, this can even lead in practice to a premature separation of the boundary layer [38], referred to as *Grid Induced Separation* (GIS).

Several modifications and improvements based on the initial DES formulation have been proposed to try to get rid of the MSD and GIS issues in practical DES. Two of these approaches are detailed below, namely the *Delayed Detached Eddy Simulation* (DDES) and the *Zonal Detached Eddy Simulation* (ZDES) approaches.

The Delayed DES (DDES) approach:
Spalart *et al.*[50] proposed a first modification of the DES97 model by introducing a specific shielding function based on a marker of the wall region. The shielding function introduced in relation (7), denoted f_d by the authors is defined as:

$$f_P = f_d = 1 - \tanh\left(\left[8r_d\right]^3\right), \qquad \text{with} \quad r_d = \frac{\nu_t + \nu}{\|\nabla\mathbf{u}\|\kappa^2 d_w^2} \tag{10}$$

where ν_t and ν are respectively the turbulence and molecular viscosities, d_w is the distance to the closest wall and $\|\nabla\mathbf{u}\| = \sqrt{u_{i,j}u_{i,j}}$. The new parameter r_d is a slightly modified version of the original parameter r appearing in the SA model, which is a good marker of the wall region ($r_d = 1$ in a log layer).

Although this method is still of common use, it is worth noting that the proposed shielding function f_d is not able to properly ensure the RANS behavior when the grid is

significantly refined in the x direction (typically when $\Delta x < 0.3\delta$ [18]). This is a major shortcoming of this approach, especially when grid refinement is required to properly resolve the separated areas, or when isotropic grids are used, such as in the case of hierarchical Cartesian grids. The use of such grids are today of growing interest, since they are notably used in the framework of the immersed boundary methods and Lattice Boltzmann methods. In such not so uncommon cases, a dramatic destruction of the eddy viscosity occurs, leading to an artificial flow laminarization, even on very simple test cases such as a zero pressure gradient flat plate (see [24]).

Moreover, the DDES is also generally observed to delay significantly the formation of physical instabilities in shear layers, due to a too large extent of the grey area. These two points have been addressed in detail by Deck & Renard [18] in order to develop an improved shielding function in the framework of the Zonal DES approach (ZDES). The branch of their approach which allows an automatic switch between the RANS and LES behaviors is detailed below.

The ZDES mode 2 (2020) approach:
This approach introduces an enhanced shielding function with the following objectives:

1. Detect and protect in RANS mode the inner region of the boundary layer
2. Detect and protect in RANS mode the outer/wake region of the boundary layer
3. Ensure a rapid switch to LES in shear layers

For that purpose, three normalized sensors are used. The first one is reminiscent of the DDES approach: a slightly modified version of r_d detects the inner region of the attached boundary layers. A second sensor $\mathcal{G}_{\tilde{\nu}}$ aims at detecting the wake region of the boundary layer, by monitoring the decay of the pseudo-viscosity in the wall-normal direction. Finally a third sensor $\mathcal{G}_\Omega$ aims at detecting flow separation by monitoring the wall-normal derivative of the vorticity. The expressions of these three sensors are:

$$r_d = \frac{\tilde{\nu}+\nu}{\|\nabla\mathbf{u}\|\kappa^2 d_w^2}; \quad \mathcal{G}_{\tilde{\nu}} = \frac{25}{\|\nabla\mathbf{u}\|\kappa d_w}\max\left(0, -\frac{\partial\tilde{\nu}}{\partial n}\right); \quad \mathcal{G}_\Omega = \frac{\partial\|\mathbf{\Omega}\|}{\partial n}\sqrt{\frac{\tilde{\nu}}{\|\nabla\mathbf{u}\|^3}} \tag{11}$$

where $\dfrac{\partial\tilde{\nu}}{\partial n} = \nabla\tilde{\nu}\cdot\mathbf{n}$ is the wall normal derivative of the pseudo viscosity, with $\mathbf{n}$ the unit vector normal to the wall[3] and $\|\mathbf{\Omega}\|$ is the norm of the vorticity vector.
Using these sensors, several shielding functions are defined. First, the f_d function from the DDES is re-used to shield the inner region of the attached boundary layers:

$$f_d = 1 - \tanh\left([8r_d]^3\right) \tag{12}$$

A second function is introduced to detect the wake region of the boundary layer and enhance the overall shielding of the approach:

$$f_{P2} = \frac{f_d\left(2.5\, r_d\right)}{f_d\left(r_d\right)} f_d\left(\mathcal{G}_{\tilde{\nu}}\right) \tag{13}$$

[3]In practice, the unit vector normal to the wall can be obtained thanks to the wall distance gradient: $\mathbf{n} = \frac{\nabla d_w}{|\nabla d_w|}$

Since this function is in practice not able to distinguish the wake region of the boundary layer from the beginning of a shear layer, a third function, referred to as the inhibition function is introduced. Its role is to disable the RANS shielding when separation is detected and allow a proper switch to LES in these regions:

$$f_R\left(\mathcal{G}_\Omega\right) = \begin{cases} 1 & \text{if } \mathcal{G}_\Omega \leq 0.03 \quad \text{or } \|\mathbf{\Omega}\| < 0.8\|\mathbf{u}\| \\ \frac{1}{1+\exp\left(\frac{6\alpha}{\alpha^2-1}\right)} & \text{if } 0.03 < \mathcal{G}_\Omega < 0.04 \quad \text{with } \alpha = 7 - 200\,\mathcal{G}_\Omega \\ 0 & \text{if } \mathcal{G}_\Omega \geq 0.04 \end{cases} \tag{14}$$

Using the three functions f_d, f_{P2} and f_R, the final ZDES shielding function is:

$$f_P = f_d\left(1 - \left(1 - f_{P2}\right) f_R\right) \tag{15}$$

It is also worth noting that the ZDES approach differs from the DDES by the use of an improved LES cutoff length and modified f_{v1}, f_{v2} and f_w functions in the SA transport equation. These modifications are very important in order to allow a rapid switch from the RANS to the LES behavior and minimize the extent of the grey area. For that purpose, two boolean functions are introduced:

$$\text{test}_\Delta = \begin{cases} 0 & \text{if } f_d \leq 0.8 \text{ or } \left(1 - \left(1 - f_{P2}\right) f_R\right) \leq 0.8 \\ 1 & \text{otherwise} \end{cases} \tag{16}$$

$$\text{test}_w = \begin{cases} 0 & \text{if } f_d \leq 0.2 \text{ or } \left(1 - \left(1 - f_{P2}\right) f_R\right) \leq 0.2 \\ 1 & \text{otherwise} \end{cases} \tag{17}$$

Using these two boolean functions, the improved cutoff length and modified functions (denoted by a prime) reads:

$$\Delta = \left(1 - \text{test}_\Delta\right)\Delta_{max} + \text{test}_\Delta \Delta_{LES} \tag{18}$$

$$f'_{v1} = \left(1 - \text{test}_\Delta\right) f_{v1} + \text{test}_\Delta f_{v1,mode1} \tag{19}$$

$$f'_{v2} = \left(1 - \text{test}_\Delta\right) f_{v2} + \text{test}_\Delta f_{v2,mode1} \tag{20}$$

$$f'_w = \left(1 - \text{test}_w\right) f_w + \text{test}_w\left[100\left(1 - \text{test}_\Delta\right) + \text{test}_\Delta f_{w,mode1}\right] \tag{21}$$

where the functions borrowed from the mode 1 from the ZDES are designed to allow a faster switch in LES mode:

$$\begin{array}{lll} \text{If } d_w > C_{DES}\Delta_{LES} & \text{then} & f_{v1,mode1} = 1\,;\, f_{v2,mode1} = 0\,;\, f_{w,mode1} = 1 \\ & \text{else} & f_{v1,mode1} = f_{v1}\,;\, f_{v2,mode1} = f_{v2}\,;\, f_{w,mode1} = f_w \end{array} \tag{22}$$

The length Δ_{max} is the largest dimension of the local grid cell given in relation (9) and Δ_{LES} is a typical LES cutoff length. Two expressions are possible for this quantity. The first one is the definition often used in LES:

$$\Delta_{LES} = \Delta_{vol} = \left(\Delta x\,\Delta y\,\Delta z\right)^{\frac{1}{3}} \tag{23}$$

The second one is a flow-dependent length, introduced in [13] to allow the amplification of physical instabilities in shear layers, even when the spanwise grid resolution Δz is significantly larger than Δx and Δy:

$$\Delta_{LES} = \Delta_\omega = \sqrt{N_x^2\Delta_y\Delta_z + N_y^2\Delta_x\Delta_z + N_z^2\Delta_x\Delta_y} \tag{24}$$

where $\mathbf{N} = \boldsymbol{\Omega}/\|\boldsymbol{\Omega}\|$ is a unit vector that provides the orientation of the vorticity vector.

An example of the application of the ZDES mode 2 (2020) approach to the simulation of a three-element high-lift airfoil will be presented in Section 4.4.3. The results obtained using ZDES in the framework of the Navier-Stokes equations resolved on body-fitted grids will be compared to the results from the same modeling approach, combined with a wall model and implemented in an LBM solver in an octree Cartesian grids framework. The results will also be compared to those from a wall-resolved LES and to experimental data.

4 Wall models for Hybrid RANS/LES methods

Important CPU costs may still arise in hybrid RANS/LES simulations, even when near-wall turbulent fluctuations are modeled. Indeed, the steep mean velocity gradients near the wall still require very fine grid resolutions for accurate representation, leading to a significant increase in the number of grid points. This fine near-wall grid resolution (typically $\Delta y^+ \simeq 1$) also involves a drastic reduction in the time step dictated by the CFL condition. As a result, it becomes of common practice to use coarser grid resolutions near the walls and rely on wall models in the first grid cells to provide the expected flow variables values. These models are designed to capture the near-wall behavior of turbulent flows without explicitly discretizing the inner part of the boundary layer, which would be computationally prohibitive in many practical applications. Over the years, various wall modeling approaches have been developed, ranging from simple algebraic laws to more advanced models based on the local solution of Ordinary Differential Equations (ODE). This section presents a non-exhaustive description of some these approaches, as well as important implementation practices that ensure an appropriate numerical behavior of the wall models.

4.1 Principle of wall models

In practice, the values of the flow variables are first interpolated at a so-called interpolation point (denoted IP in the following) in the fluid above the wall. They are then used as input data for the wall model to estimate the skin friction. The numerical implementation of the wall model follows two main approaches. The first one is particularly well-suited for finite-volume methods on body-fitted grids. In this case, the wall law provides appropriate values for the wall shear stress, which are then directly applied to impose the numerical fluxes at the interfaces of the wall cells (e.g., [6, 64, 29, 28, 11]), see Figure 1, left. The second approach, known as the direct forcing [39], uses the wall law to set the values of the field variables in the near-wall cells, see Figure 1, right. This method is particularly well-suited for Immersed Boundary Methods (IBM), where solid walls are embedded within the computational grid. These methods are gaining interest, especially when combined with hierarchical Cartesian grids, as they allow for automatic grid generation, maintain high grid quality, and support the use of accurate numerical methods [54, 9]. They are also particularly useful in the context of Lattice-Boltzmann Methods (LBM), which are usually based on Cartesian lattices [35, 7, 21, 23, 24]. Nonetheless, specific finite-volume IBM implementations also rely on applying the wall law through numerical fluxes at the

wall, using a strategy where the body surface is represented with polyhedral cut cells that have appropriate intersections (e.g. [8, 54]).

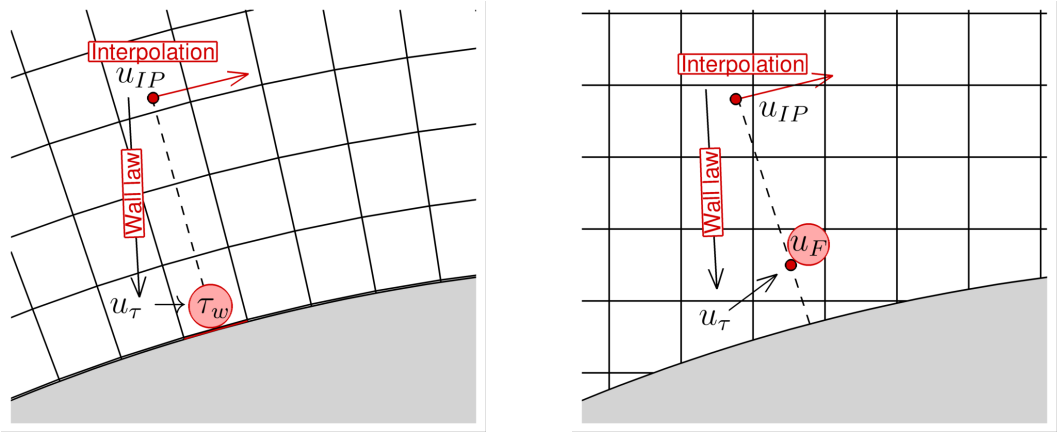


Figure 1: Schematic representation of a wall law applied using wall shear-stress imposition in a body-fitted framework (left) and using a direct forcing approach in an immersed boundary framework (right).

4.2 Classical wall models

4.2.1 ODE-based wall models

These models are based on the resolution of the so-called Thin Boundary Layer Equations (TBLE - *e.g.* [64, 6, 16, 8]), which are a simplified version of the averaged Navier-Stokes equations. For the sake of clarity, we will restrict ourselves to the $x-y$ frame linked to the wall, with x and y the streamwise and wall-normal directions, respectively[4]. The TBLE are most commonly written and solved in their steady-state incompressible form:

$$u\frac{\partial u}{\partial x} + v\frac{\partial u}{\partial y} + w\frac{\partial u}{\partial z} = -\frac{1}{\rho}\frac{\partial p}{\partial x} + \frac{\partial}{\partial y}\left((\nu + \nu_t)\frac{\partial u}{\partial y}\right) \tag{25}$$

where, for the sake of clarity, u, v and w will now denote respectively the tangential, wall-normal and spanwise velocity components.

With a proper closure for the eddy viscosity ν_t, this TBLE system can be solved directly on an auxiliary refined grid between the wall and the interpolation point. In order to minimize the potential additional cost of this resolution, this auxiliary grid often consists of linelets normal to the wall, aligned with the forcing and interpolation points.

The introduction of the streamwise pressure gradient and convective terms in the TBLE is often responsible for numerical instabilities and/or estimation issues, so that specific numerical treatments are required to include them in the TBLE system (see *e.g.* [5]). For that reason, most of the TBLE approaches rely in practice on the assumption of

[4]The general expressions of the wall-normal and tangential velocity components are respectively obtained as: $u_n = \mathbf{u}\cdot\mathbf{n}$ and $u_t = \mathbf{u}\cdot\mathbf{t}$ where $\mathbf{n}$ is the unit vector normal to the wall and the unit vector tangential to the wall is obtained as $\mathbf{t} = \dfrac{\mathbf{u} - u_n\cdot\mathbf{n}}{|\mathbf{u} - u_n\cdot\mathbf{n}|}$

equilibrium between the convection and pressure gradient terms leading to:

$$\frac{\partial}{\partial y}\left(\left(\nu+\nu_t\right)\frac{\partial u}{\partial y}\right)=0 \tag{26}$$

The numerical resolution of this Ordinary Differential Equation requires a closure for the eddy viscosity ν_t. Several variants are found in the literature, ranging from a simple mixing length model [64, 6, 8], to the resolution of an additional one-dimensional simplified SA transport equation [5, 58, 37].

The mixing length model reads as follows:

$$\nu_t = f_{VD}\,\kappa y u_\tau \tag{27}$$

where f_{VD} denotes the traditional Van-Driest near-wall damping function

$$f_{VD} = \left(1-\exp\left(-y^+/A^+\right)\right)^2 \tag{28}$$

where a typical range for the damping constant is $A^+ = 19-26$.

In the second approach (see for instance [5, 58, 37]), the eddy viscosity is computed by resolving the following simplified 1D equation, derived from the Spalart-Allmaras transport equation for the pseudo eddy-viscosity $\tilde{\nu}$:

$$\frac{\partial\tilde{\nu}}{\partial t} = c_{b1}\frac{\partial u}{\partial y}\tilde{\nu} + \frac{1}{\sigma}\left\{\frac{\partial}{\partial y}\left[\left(\nu+\tilde{\nu}\right)\frac{\partial\tilde{\nu}}{\partial y}\right] + c_{b2}\left(\frac{\partial\tilde{\nu}}{\partial y}\right)^2\right\} - c_{w1}f_w\left[\frac{\tilde{\nu}}{d_w}\right]^2, \tag{29}$$

The different constants and functions involved in (29) are those from the classical SA model [51]. The eddy viscosity ν_t is then classically computed as $\nu_t = f_{v1}\tilde{\nu}$.

It is worth noting that a similar strategy can be applied to the the energy equation, in order to obtain an additional ODE for the temperature (*e.g.* [37]).

4.2.2 Example: application to the tandem cylinder test case

This test case is the well-known tandem cylinder configuration, introduced in the framework of the BANC workshop series (see [31] for a review). Therefore, we consider the flow around two cylinders of diameter $D = 57.15$ mm placed in a tandem arrangement, with a gap of $3.7D$ between their respective axis. The flow velocity is 44 m/s leading to a diameter-based Reynolds number of $Re_D = 166,000$. This is a classical aeroacoustic test case where the far-field noise prediction is highly dependent on whether the interaction of the upstream cylinder wake with the downstream cylinder is accurately predicted or not. An extensive validation campaign has been performed by NASA on this configuration, in their aerodynamic and aero-acoustic wind tunnels [26, 27, 41], so that experimental data are available for comparison. This configuration has also been retained for noise reduction studies in the framework of the EU/China collaborative project IMAGE. We present here only a brief overview of some of our results obtained on this configuration in the framework of this project, using ZDES on cartesian octree grids. A spanwise extent of $4D$ with periodicity conditions was retained for the study. The near-wall grid resolution was set to $5.9\times10^{-3}D$, leading to a computational grid composed of 26 million points. The interested reader may refer to [58] for more details and additional configurations

with flow-through fairings used for noise reduction. In these simulations, the equilibrium TBLE model (30) has been used, combined with the 1D SA equation (29) for the eddy viscosity. Overall, the use of this wall model was found to yield the best quality of the results, compared to other wall models.

Figure 2 presents the instantaneous spanwise vorticity component and resolved 2D TKE maps in the central plane, compared to the PIV measurements. Overall, the shear layer characteristics and separation location are well predicted by the numerical simulation. The main TKE spot in the gap is also well located, although it presents a slightly higher level. Figure 3 shows the wall-pressure Power Spectral Density (PSDs) obtained, respectively, at 135° on the upstream cylinder and 45° on the downstream cylinder. Again, a good agreement between the simulaton and the measurements is obtained, for both the overall magnitude and the main peak tonal frequency. On the upstream cylinder, a faster decay of the PSD is observed in the simulations above St$\simeq$1. This can probably be explained by the use of the wall model with a moderate grid resolution, which delays a bit the formation of instabilities near the separation point. Finally, the far-field pressure spectra (obtained using a permeable FW-H method) are displayed in Figure 3 (right) and compared to NASA's microphone measurements in the QFF wind tunnel. Overall, a good agreement with the measurements is observed, although the first harmonic of the main tonal peak is over-predicted.

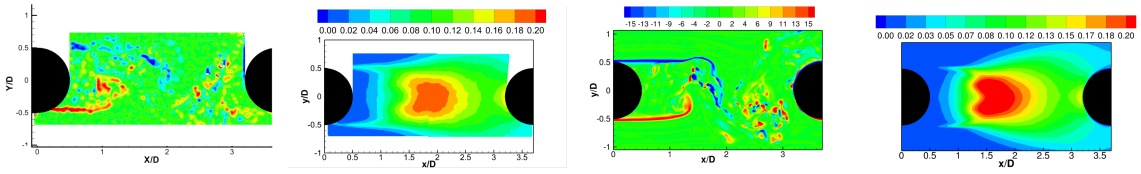


Figure 2: Tandem cylinder test case: instantaneous spanwise vorticity and 2D resolved TKE contours. Left: NASA PIV measurements in the BART facility; Right: ZDES on octree cartesian grid with the equilibrium SA-TBLE model.

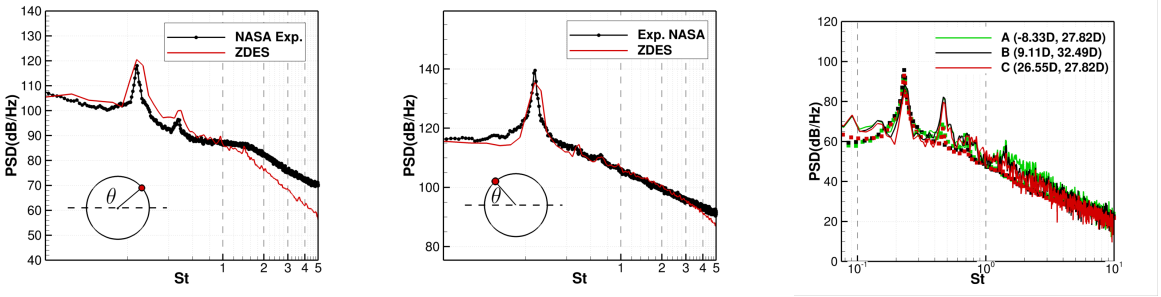


Figure 3: Tandem cylinder test case: wall pressure PSD at $\theta = 135°$ on the upstream cylinder (left) and at $\theta = 45°$ on the downstream one (center). Right: far-field noise spectra (simulation in solid line, NASA measurements as symbols).

4.2.3 Algebraic wall models

Let us consider again the steady equilibrium boundary layer equation, *i.e.* assuming equilibrium between the convection and pressure gradient terms. By integrating Equation (26) along y and by remembering that the friction velocity is expressed as $u_\tau = \sqrt{\nu \left.\frac{\partial u}{\partial y}\right|_{y=0}}$, we obtain the following expression, imposing a constant value to the total shear stress:

$$(\nu + \nu_t) \frac{\partial u}{\partial y} = u_\tau^2 \tag{30}$$

Very close to the wall ($y^+ \leq 11.5$), the viscous effects are predominant and ν_t can be neglected in (26). This leads to the following linear behavior of the velocity field:

$$u^+ = y^+, \qquad \text{for } y^+ \leq 11.5 \tag{31}$$

For $y^+ > 30$, the turbulent stresses become dominant compared to the viscous stresses and a dimensional analysis yields $\nu_t/\nu = \kappa y^+$. With this assumption, integrating relation (30) recovers the well-known logarithmic law of the wall:

$$u^+ = \frac{1}{\kappa} \ln(y^+) + B \tag{32}$$

where standard values[5] for the Kármán constant and the additive constant are $\kappa = 0.41$ and $B = 5.2$ respectively.

Several methods make it possible to derive a continuous expression for the velocity expression, in order to account for the buffer layer between the linear and logarithmic regions. For instance, Musker [40] proposed an empirical blending for the eddy viscosity between the linear region close to the wall and the logarithmic region. Using (30), this yields an algebraic expression for the wall-normal derivative of tangential velocity and, after integration, to a continuous expression for the velocity distribution from the wall to the logarithmic region.

In a similar way, Allmaras *et al.*[4] derived a specific wall law, which is an analytical solution of the equilibrium boundary layer equations (30), closed by the Spalart-Allmaras model. Therefore, the authors assume that the eddy viscosity is a near-wall solution of the Spalart-Allmaras transport equation:

$$\nu_t = \nu \chi f_{v1}(\chi) \tag{33}$$

where we recall that $\chi = \tilde{\nu}/\nu$ is the normalized pseudo-viscosity and $f_{v1} = \chi^3/\left(\chi^3 + c_{v1}^3\right)$ [51]. Since, by construction, χ evolves as $\chi = \kappa y^+$ near the wall, Equation(30) can be re-written, in wall units, as:

$$\frac{\partial u^+}{\partial y^+} = \frac{c_{v1}^3 + (\kappa y^+)^3}{c_{v1}^3 + (\kappa y^+)^3 (1 + \kappa y^+)} \tag{34}$$

The analytical solution of this equation, usually referred to as the Spalart-Allmaras (SA) wall model, is [4]:

$$\begin{aligned} u_{SA}^+ &= c_1 \ln((y^+ + a_1)^2 + b_1^2) - c_2 \ln((y^+ + a_2)^2 + b_2^2) \\ &- c_3 \ \text{ArcTan}[y^+ + a_1, b_1] - c_4 \ \text{ArcTan}[y^+ + a_2, b_2] + \overline{B}, \end{aligned} \tag{35}$$

[5]The universality of the values of κ and B is still an open debate.

where ArcTan$[x, y]$ is the Mathematica function that gives the arc tangent of y/x, taking into account which quadrant the point (x, y) is in.
The constant parameter values are :

$$\begin{array}{lll} \overline{B}=5.0333908790505579 & , & \\ a_1=8.148221580024245 & , & a_2=-6.9287093849022945 \\ b_1=7.4600876082527945 & , & b_2=7.468145790401841 \\ c_1=2.5496773539754747 & , & c_2=1.3301651588535228 \\ c_3=3.599459109332379 & , & c_4=3.6397531868684494 \end{array}$$

Relation (35) is of great interest for all the numerical approaches based on the SA turbulence model, such as for instance the ZDES approach, because it offers a full consistency between the wall law and the turbulence model. For that reason, the rest of this manuscript will mainly focus on the use of this specific wall model. However, it is worth noting that many other works have been devoted to the derivation of algebraic expressions for the near-wall velocity field. The interested reader may for instance refer to the works by Spalding [52], Reichardt [43] or Wilhelm *et al.*[65]. Some more advanced models also include non-equilibrium effects by accounting for the pressure gradient[6] *e.g.* [3, 66].

Most of the algebraic wall models focus on the derivation of a law for the tangential velocity component. It is also necessary to provide appropriate values at the forcing point for the wall-normal velocity component and the other primitive variables. For that purpose, the common practice is to simply assume a linear behavior of the wall-normal velocity, a constant wall-normal pressure variation near the wall, Crocco-Busemann relationship for the temperature field (*e.g.* [54]) and the perfect gas state law for density.

4.3 Linearization approach

In all cases, it is worth noting that the near-wall velocity expression given by the wall model introduces steep velocity gradients in the first grid cells, regardless of the numerical implementation. However, nothing ensures that the numerical scheme behaves properly when grid resolutions typical of wall-modeled simulations are used near the walls, especially when low-order numerical scheme are used. This is the main reason why a lack of grid convergence is generally observed in wall-modeled numerical simulations, with a non-monotonous and unpredictable behavior of the solution accuracy when the grid is refined. A possible solution to overcome this inappropriate behavior relies on a linearization technique of the wall model velocity expression, that will be further detailed below. Before fully describing this wall model linearization technique, we will analyze and quantify below the numerical error that may arise if the wall model were applied directly to the near-wall points.

4.3.1 Numerical error Analysis

Let us first recall that, according to Relation (30), the total shear stress is expected to be constant along the wall-normal direction, *i.e.* $\tau(y) = u_\tau^2$, with $\tau = (\nu + \nu_t)\,\frac{\partial u}{\partial y}$.

[6] As it is the case for the full TBLE equation, accounting for the pressure gradient may in some case lead to numerical instabilities and require specific numerical stabilizations.

In a second-order accurate finite-volume or finite-difference solver, with a uniform wall-normal grid resolution Δy, this quantity may usually be evaluated as:

$$\tau_{num}(y) = (\nu + \nu_t(y)) \frac{u(y+\Delta y) - u(y-\Delta y)}{2\Delta y} \tag{36}$$

Therefore, the relative numerical error committed on the shear stress with respect to its theoretical value u_τ^2, may then be expressed as:

$$\varepsilon_\tau \quad = \quad \left| \frac{\tau_{num} - u_\tau^2}{u_\tau^2} \right| \tag{37}$$

In the specific case of the SA wall model, we get the following expression for the local shear stress error [56]:

$$\varepsilon_\tau \quad = \quad \left| \frac{1 + \kappa y^+ f_{v1}\left(\kappa y^+/\nu\right)}{2\Delta y^+} \left[u_{SA}^+(y^+ + \Delta y^+) - u_{SA}^+(y^+ - \Delta y^+) \right] - 1 \right| \tag{38}$$

Figure 4 presents the corresponding error map, as a function of the grid resolution in wall units Δy^+ and the normalized wall-normal coordinate $y^+/\Delta y^+$, for arbitrary representative values[7] of the input parameters ν and u_τ. On the one hand, it appears that, except for very fine grid resolutions (typically $\Delta y^+ < 5$), a very high error is present for the first near-wall points ($y^+ < 2\Delta x$). Therefore, imposing directly the velocity value predicted by the wall law at these first grid points near the wall may result in a large prediction error on the shear stress (by more than 100% at the first point), which is clearly not acceptable. On the other hand, the error decreases nicely as the ratio $y^+/\Delta y^+$ increases, *i.e.* further away from the wall. Therefore, it appears clever to modify the near-wall behavior of the velocity field in order to satisfactorily match the region where the shear stresses are resolved with a lower error level. This is precisely the idea of the linearized wall model presented in the next section.

4.3.2 Linearized wall model

It appears clearly from the above analysis, that the direct use of relation (35) at the forcing point ($y = y_F$) may lead in most cases to the implicit introduction of too steep velocity gradients, not supported by the grid when using a low-order numerical scheme. For this reason, Capizzano [8] introduced the idea of velocity linearization in order to ensure an acceptable reconstruction of the wall-normal velocity derivative in the numerical solver. Indeed, the proposed modification relies on the idea that in the framework of a second-order finite-volume scheme, *a cell near the wall can see only linear variations of the flow variables* [8]. This idea was later on revisited by Tamaki *et al.*[54], who proposed a dedicated modification of the SA turbulence model in order to preserve the near-wall shear stress balance when the wall law is linearized. In their approach, the tangential velocity component u_F at the forcing point F is re-written as the following the linearized SA wall law[8]:

$$u_F^+ = u_{SA}^+(y_{IP}^+) - \left(y_{IP}^+ - y_F^+\right) \frac{\partial u_{SA}^+}{\partial y^+}\left(y_{IP}^+\right) \tag{39}$$

[7] Due to the wall units scaling used, the computed values of ε_τ do not depend on the values of ν and u_τ

[8] In the original works of Capizzano [8] a TBLE model was used instead of the SA wall model.

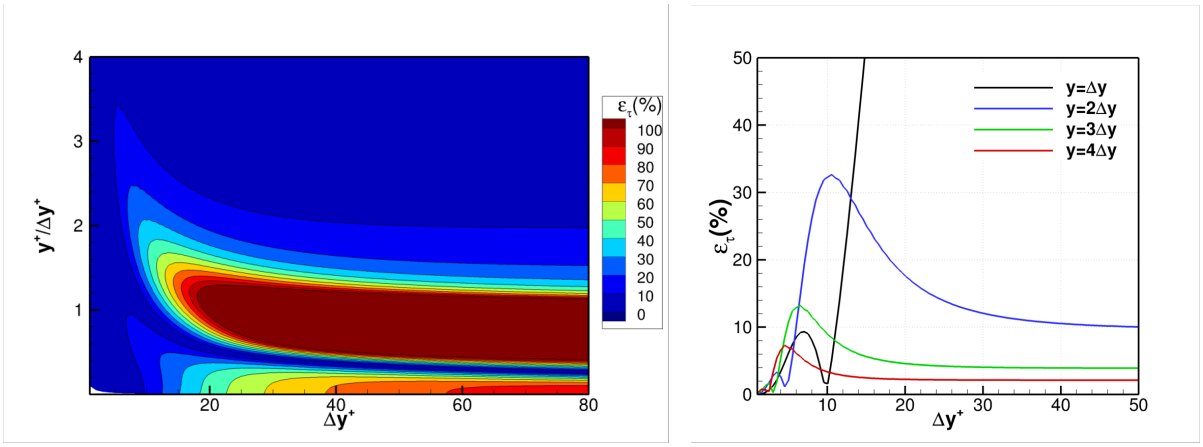


Figure 4: Relative total shear-stress term error, expressed in percent (*i.e.* $100\varepsilon_\tau$).

where we recall that "IP" denotes the reference interpolated point used to predict the local value of u_τ. The expression of the tangential velocity u^+_{SA} and of its wall-normal derivative $\partial u^+_{SA}/\partial y^+$ are given by their algebraic expressions (35) and (34), respectively.

Relation (39) therefore ensures a linear behavior of the velocity below $y = y_{IP}$, with a wall-normal velocity derivative consistent with the wall law at $y = y_{IP}$, where the wall-normal velocity gradient is expected to be much lower and better supported by the grid. A typical value for the interpolated point wall distance is $y_{IP} = 3\Delta y$. According to Figure 4, this brings the shear-stress error to an average level of about 5%. In [56], we propose a more advanced linearization method, which provides a dynamic estimate of the optimal linearization distance in order to further minimize the shear stress error, regardless of the local grid resolution.

4.3.3 Eddy viscosity modification

As detailed by Tamaki *et al.*[54], a near-wall modification of the SA model is required when using the velocity linearization process (39), in order to ensure the conservation of the total shear stress (relation (30)). In [54], a near-wall modification of the SA f_{v1} damping function is proposed to do so. For any point at a distance y from the wall, the eddy viscosity is then evaluated as:

$$\nu_t = r_{lin} f_{v1}\left(r_{lin}\chi\right)\tilde{\nu} \qquad , \qquad \text{with } \chi = \frac{\tilde{\nu}}{\nu} \tag{40}$$

instead of the classical expression $\nu_t = f_{v1}\left(\chi\right)\tilde{\nu}$. Here, f_{v1} still denotes the classical damping function of the standard Spalart-Allmaras turbulence model and the modification is only effective by introducing the distance scaling factor r_{lin}, defined as:

$$r_{lin} = \frac{y_{IP}}{y} \text{ if } y < y_{IP}, \tag{41}$$

$$r_{lin} = 1 \text{ elsewhere.} \tag{42}$$

It is straightforward to show that in the near-wall region, when the pseudo-viscosity evolves as $\tilde{\nu}(y) = \kappa u_\tau y$, relation (40) simplifies as $\nu_t(y) = \nu_t(y_{IP})$ if $y < y_{IP}$. Therefore,

this ensures a constant total shear stress when $y < y_{IP}$, *i.e.* when the velocity profile is forced to evolve linearly according to relation (39), with a constant value of its wall-normal derivative.

4.4 Examples

4.4.1 Zero pressure gradient flat plate

First, in order to illustrate the benefit of the linearization method over the standard forcing method, we present below RANS simulations of the well-documented zero pressure gradient test case from the Turbulence Modeling Resource [2]. We consider the turbulent flow developing over a flat plate, for a Reynolds number value $Re_L = 5 \times 10^6$ based on the half length of the plate L. A second-order accurate finite volume solver is used for this study (see *e.g.* [58] for details), with the SA wall law retained for the wall-modeled simulations performed on octree Cartesian grids. Figure 5 compares the predicted skin friction coefficient along the flat plate, for different near-wall grid resolutions. The C_f predicted by the CFL3D solver on a refined grid is used as reference. On the one hand, it appears clearly that no grid convergence trend is obtained with the standard direct forcing approach: a significant over-prediction of the skin friction coefficient is obtained, regardless of the near-wall grid resolution. It is also noticeable that the error on C_f is even increasing when the grid is refined. On the other hand, the linearized approach leads to a much better agreement with the reference, while an overall grid convergence trend is observed.

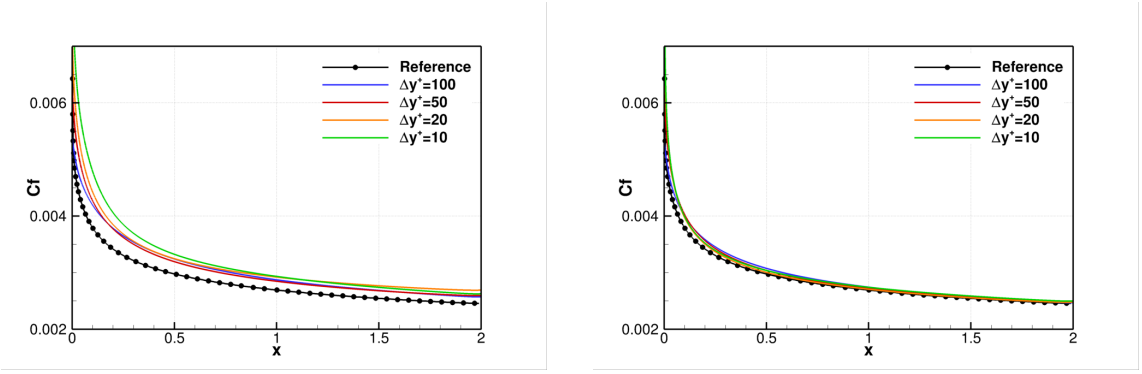


Figure 5: Skin-friction coefficient for the zero pressure gradient test case. Left: results from the standard direct forcing method; Right: Results with the linearized direct forcing method.

4.4.2 ZDES of a simplified landing gear

This second test case has been extensively studied in the framework of the INVENTOR H2020 research project. It concerns the prediction of the aerodynamic and acoustic field of a landing gear configuration including realistic components responsible for high acoustic levels (torque link and brakes). Because of the geometrical complexity of the configuration, an immersed boundary method on Cartesian grids has been used. The simulations were carried out using the FUNk solver, with the ZDES mode 2 (2020) approach presented

in Section 3 and combined with the linearized SA wall law. Figure 6 shows the studied configuration and the octree grid used. Note that the upper wall, not shown in the figure, is also taken into account by a slip boundary condition. The flow conditions match those of corresponding experiments carried out at TUD in their Acoustic wind tunnel, with an upstream velocity of 35 m/s and a wheel diameter D =150mm. This figure also displays a snapshot of the resulting flow, where we can appreciate the complexity of the wake developing downstream of the torque-link. The analysis of the dilatation field reveals that the main acoustic sources are located at the torque link (more precisely at its circular orifices) and in the brakes area.

Figure 7 presents a brief comparison of the predicted mean velocity and RMS velocity fluctuations against TUD's PIV measurements. Overall, we observe a good agreement between the simulation and the experiment, which indicates that the attached and separated flow regions are correctly predicted. Finally, this figure also displays a comparison of the predicted acoustic field (using a solid FW-H method) with the microphone array measurements. Again, there appears to be a fair agreement between the simulation and the experiment. For a more detailed comparison, the interested reader may refer to [60], where additional cases including porous fairings for noise reduction are also considered.

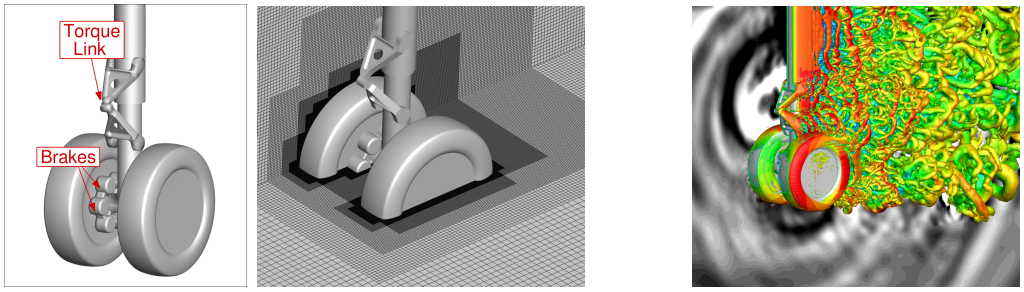


Figure 6: Landing gear configuration. Left: geometry and grid; Right: iso-Q surface, colored by velocity magnitude and dilatation field (grey contours).

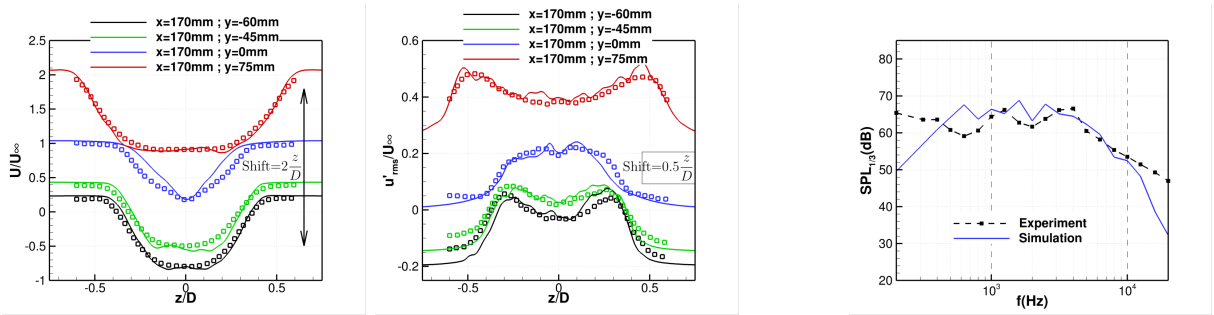


Figure 7: Landing gear configuration. Left: Mean and RMS velocity profiles at x/D=1.13); Right: Sound pressure level prediction at the central flyover microphone for the baseline configuration (third-octave band dB, $p_{ref} = 2 \times 10^{-5}$ Pa)

4.4.3 ZDES of the F16 high-lift airfoil configuration

It is worth noting that all the previous approaches are in practice not limited to the framework of a Navier-Stokes solver. Indeed, several works have been carried out to implement

and evaluate the linearized SA wall law and the ZDES approach in the framework of a Lattice Boltzmann Method [23, 24]. As an illustration we report below an extract of the works by Husson *et al.*[22] dealing with the simulation of the LEISA2 configuration with this methodology implemented in the ProLB LBM solver [1].

The high-lift airfoil under consideration is the DLR F16 wing profile, which is the second benchmark case from the BANC workshop high-lift section. Its retracted chord is c =0.3 m. Based on the experimental campaign led during the LEISA2 project [36],the free-stream conditions are M=0.178 and $Re_c = 1.23 \times 10^6$. The angle of attack is 6.15°. A large experimental database includes static pressure, PIV maps, LDV measurements on several rakes and microphone array acoustic data [36]. Wall-resolved LES results on a very refined grid (2.6 billion points) are also available as an additional numerical reference [57].

Two simulations using the ZDES mode 2 (2020) turbulence model are here compared briefly to the reference results (see [22] for a more detailed comparison): the first one is performed on a body-fitted grid, using a Navier-Stokes solver based on second-order finite-volume scheme. The second one is done using the ProLB solver, where the LBM equations are solved on a set of octree Cartesian grids. In this case, the wall boundaries are accounted for by the use of an immersed boundary method, combined with the use of the linearized SA wall model presented previously. Hence, these two simulations use the same turbulence model, in very different numerical frameworks. In both cases, the grid is significantly refined in the slat cove region only, since it represents the main acoustic source in such a configuration. This makes it possible to save a lot of computational resources compared to the wall-resolved LES (65 million points for the ZDES-NS and 88 million points for the ZDES-LBM, compared to the 2.6 billion points required for the WRLES). In both cases, a spanwise extent of about 0.16 chord is considered[9], with periodicity boundary conditions.

Figure 8 presents instantaneous snapshots of the flow in the slat cove. For both simulations, the main characteristic flow features of the flow inside a slat cove (*e.g.* [15, 59]) are well recovered: (i) a large recirculation bubble occurs in the slat and is surrounded by a large shear layer originating from the cusp; (ii) a fast 2D/3D transition occurs in this shear layer which finally impinges the upper wall; (iii) at the impingement location, large vortices are re-injected in the main recirculation bubble, while the others are strongly accelerated, convected downstream as streamwise-oriented structures and eventually interact with the trailing edge. Despite different apparent shedding frequencies at the cusp, probably due to large differences in the grid resolution in this area, the two simulations exhibit very similar behaviors, with a very fast switch from a RANS resolution of the attached boundary layers to an LES resolution of the detached shear layers.

A more quantitative comparison is presented in Figure 9, presenting the mean velocity profiles and the resolved RMS velocity fluctuations, compared to the LDV and WRLES reference results. For the sake of brevity, only one rake of data located inside the slat cove is shown here. It is worth noting that both simulations agree very well with the reference results, for both the mean and RMS values. The only difference appears to be a small shift of the shear layer in the x direction for the LBM solution, which is probably due to a too coarse resolution of the cusp geometry on the Cartesian grid. A much more exhaustive

[9]The slat chord of this airfoil is $c_s = 0.186c$. According to several studies [32, 59], a spanwise extent of about 80% of the slat chord is sufficient to properly represent the largest flow structures.

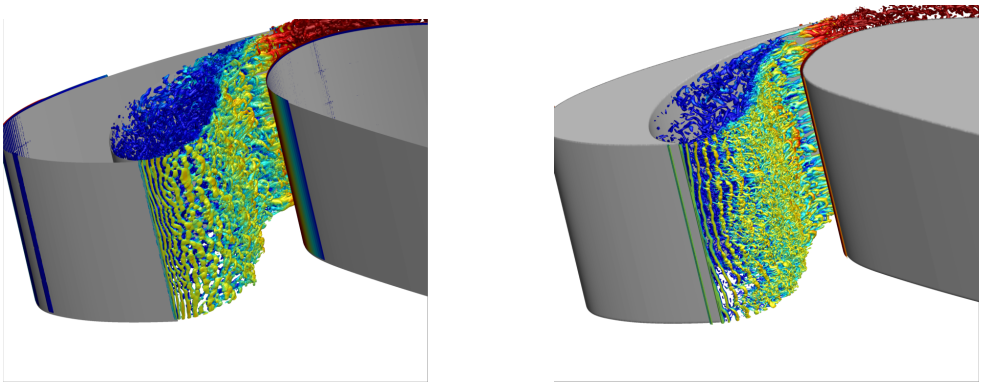


Figure 8: Comparison of iso-surfaces the Q-criterion ($Qc^2/U_\infty^2 = 5000$) in the slat cove, colored by velocity magnitude between ZDES-NS (left) and ZDES-LBM (right) simulations. LBM results courtesy of J. Husson.

comparison between the ZDES-NS and ZDES-LBM simulations is available in [22], where a spectral analysis also exhibits a nice agreement between these two approaches and shows their ability to properly capture the Rossiter-like aeroacoustic feedback loop [59] in the slat cove.

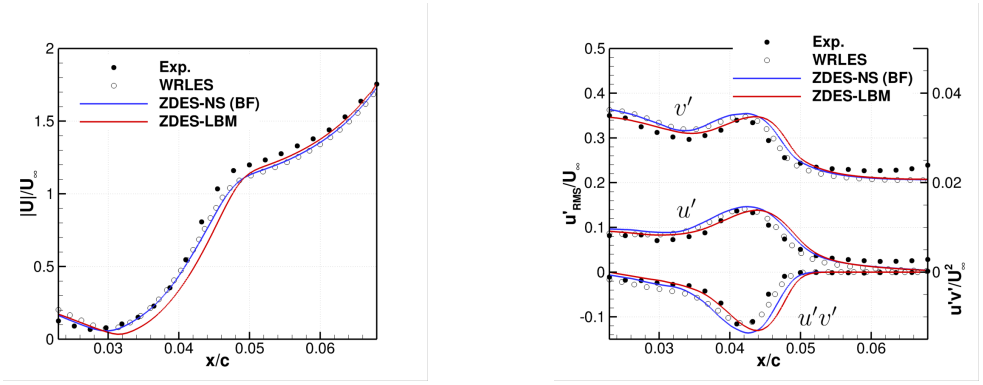


Figure 9: Mean velocity profiles (left) and resolved RMS velocity fluctuations profiles (right), compared to the reference LDV and WRLES results. The considered rake is located just upstream of the slat gap (rake 3 from [22]). LBM results courtesy of J. Husson.

5 Towards wall-modeled LES

In the previous approaches, the whole boundary layer thickness is voluntarily treated in RANS in the attached flow regions. This allows to save a lot of computational resources since the grid resolution required for RANS is much coarser than the one required for an explicit resolution of the turbulent boundary layer dynamics. However, some applications may still require an explicit resolution of the turbulent fluctuations from the TBL, such as in the presence of thick boundary layers where the TBL inner fluctuations may influence the flow physics (*e.g.* shallow separation, boundary layer self noise, acoustic waves diffusion, ...) or when their interaction with other components cannot be neglected, *e.g.* when

a propeller is significantly immersed in the boundary layer in novel Boundary Layer Ingestion (BLI) architectures. In that sense, the class of the wall-modeled LES (WMLES) methods has been introduced. These methods aim at lowering the cost of an explicit resolution of the turbulent fluctuations by resolving in LES only the outer layer of the boundary layer, while its inner layer is modeled. In a general way, this can be achieved by considering a thin layer resolved with a RANS turbulence model and/or by modeling this region with a wall model. One of these approaches, derived from the ZDES approach, will be presented below, although many other methods are found in literature since this approach still represents an open active research subject (see for instance the blending approach by Tamaki and Kawai [55] in Section 5.3).
It is worth noting that such approaches require specific inflow conditions and/or synthetic turbulence generation methods in order to develop resolved turbulent fluctuations in the outer layer. This is often the case for LES-based methods of spatially-developing boundary layers where turbulent inflow conditions have to be used to avoid the simulation over a two long streamwise extent. This point is exacerbated in WMLES because the near-wall turbulence generation mechanisms are no longer explicitly resolved, but only modeled. In practice, a WMLES with no specific turbulence generation technique would lead to a laminar solution with a poor prediction of the mean boundary layer characteristics.
Many methods have been developed to allow a quick generation of turbulent fluctuations in the boundary layer, such as the use of recycling strategies [34], the Synthetic Eddy Method (SEM) [25, 42], or the use of dedicated triggering devices (*e.g.* small vertical rods) inside the boundary layer to generate vortices [19]. All these approaches can also be combined with a dynamic forcing technique [30], to allow a quicker relaxation of the solution towards a fully-developed turbulent boundary layer. Another constraint for aeroacoustic studies is that these inflow generation methods must be as silent as possible and do not corrupt the predicted acoustic field. The full description of these approaches falls beyond the scope of the present lecture, but the interested reader may for instance refer to [19] for a more exhaustive description.

5.1 The ZDES mode 3 approach

This method represents the WMLES branch of the ZDES [17, 19]. Its general expression still follows the general definition of the hybrid lengthscale given in relation (7), where the shielding function is expressed here as:

$$f_P = \begin{cases} 0 & \text{if } d_w < d_{interface} \\ 1 & \text{otherwise} \end{cases} \tag{43}$$

This ensures a RANS behavior in the near wall region below the RANS/LES interface location $d_{interface}$ and a LES behavior in the region above this interface. A typical value for the interface height is $d_{interface} = 0.1\delta$.
In order to accelerate the generation of turbulent fluctuations and resolved Reynolds stresses, the authors recommend to modify the functions of the SA model in the LES region *i.e.* when $d_w > d_{interface}$ as:

$$f_{v1} = 1\,;\; f_{v2} = 0\,;\; f_w = 1 \tag{44}$$

The authors also proposed a regularization of the binary switch from RANS to LES by replacing the expression of f_P given in Equation (43) by a smooth expression that varies continuously from 0 to 1 when $d_w \in [0.9 d_{interface}; 1.1 d_{interface}]$ (see [44]).

In this general expression, the turbulence model acts in practice as a wall model since the full three-dimensional RANS equations are resolved for wall distances smaller than $d_{interface}$. This makes it very general, since all the physical effects such as the convection or the pressure gradients are directly accounted for. Therefore, this method made it possible to simulate high -Reynolds turbulent boundary layers under non-equilibrium effects (*e.g.* [61, 63, 62]).

However, the ZDES mode 3 approach suffers from the same CPU cost limitations as the ZDES mode 2, since near-wall grid resolutions of $y^+ \simeq 1$ are still required to properly resolve the inner layer in RANS mode. It is worth noting that since the near wall solution is computed in RANS, it an be easily coupled with a wall model in order to relax this resolution constraint. This can lead in practice to important savings of the necessary CPU resources by considering coarser near-wall grid resolutions and larger time steps. In this case, the method is in practice a three-layer approach where the total height of the boundary layer is solved by:

- A wall model applied to a thin layer (typically one or two points) of near-wall forcing points. For that purpose, one may for instance rely on the linearized SA wall law presented in Section 4.3.2.
- A second layer, below $d_{interface}$, where the turbulence model acts in RANS mode.
- The outer layer, where the turbulence model switches to its LES behavior and where the turbulent fluctuations are resolved explicitly.

5.2 ZDES of a propeller partially immersed in a turbulent boundary layer

The ZDES mode 3 approach with wall model has been retained in the framework of the ENODISE H2020 project to simulate the interaction between a thick boundary layer and a static propeller (case A1 of ENODISE database), in order to investigate the effect of the turbulent fluctuations from the boundary layer on the dynamics of the flow and noise generation around the propeller blades when the boundary layer thickness is not negligible compared to the propeller diameter.

Figure 10 presents the configuration that has been retained. It was defined to match as closely as possible the conditions of dedicated experiments carried out at University of Twente [10]. A static propeller (with a diameter $D = 0.3048$m) in vertical position is located at $x = 0$, just above a flat plate. The targeted boundary layer thickness at the propeller location is about half its diameter *i.e.* $\delta \simeq 0.15$ m. The inflow velocity is $U_\infty = 30$ m/s, so that the Reynolds number based on this boundary layer thickness is $Re_\delta \simeq 342{,}000$, or a friction Reynolds number of $Re_\tau = \delta^+ \simeq 10{,}600$. The size of the computational domain has been carefully tuned in order to ensure the targeted boundary layer thickness at the propeller location and an upstream development distance of roughly 30 times the boundary layer thickness δ_0 at the inflow. Using the empirical relation (2), an upstream distance of about 5m, with $\delta_0 = 0.08$ m $\simeq 0.26D$ has finally been

considered. The overall number of grid points required for the simulation is about 500 millions, with an average near-wall grid resolution of 50 wall units all along the flat plate ($\Delta x = \Delta y = \Delta z = 0.77$ mm). A finer grid resolution $\Delta x = 0.38$ mm is used close to the propeller. The computational domain and grid used for the study are displayed in Figure 10. It can be noted that the finest resolution is only applied in a limited region near the wall and is rapidly doubled to $\Delta x^+ \simeq 100$ in order to save computational resources in the flat plate area. At the inflow, an algebraic velocity profile is imposed, using the following composite law:

$$u^+ = u^+_{SA}(y^+) + \frac{\Pi}{\kappa} W\left(\frac{y}{\delta}\right) \tag{45}$$

where the wake function is expressed as $W\left(\frac{y}{\delta}\right) = 1 - \cos\left(\pi \frac{y}{\delta}\right)$ and the wake factor Π in relation has been tuned to ensure $u^+(y = \delta) = U^+_\infty$. In addition to this inflow condition, several vertical rods have been added at the wall near the inflow, in order to trigger the generation of resolved turbulent fluctuations in the outer part of the boundary layer. The size and spacing of the rods have been carefully tuned in order to trigger the most unstable modes of the boundary layer (see [19]). The performance of this inflow tripping strategy for the ZDES mode 3 simulation can be observed in Figure 10 (right), where the classical topology of a fully-developed turbulent boundary layer, with typical hairpin-like vortices is rapidly recovered.

An additional simulation relying on the ZDES mode 2 (2020) approach has also been carried out in order to be able to quantify the effect of the resolved boundary layer turbulence on the BL/propeller interaction in the ZDES mode 3 simulation.

Figure 11 present instantaneous visualizations of the flow for the respective ZDES mode 2 and mode 3 simulations. On the one hand, it is clear that in the ZDES mode 2 simulation, the whole boundary layer upstream of the propeller is resolved in strict RANS mode with no resolved fluctuations inside the boundary layer, while the solver switches into LES mode only in the separated areas downstream of the blades. On the other hand, the ZDES mode 3 simulation offers a partial LES resolution of the outer region of the boundary layer. In this case, the interaction between the large-scale structures of the boundary layer and the propeller lower blade is clearly visible. Some differences are also visible for the radiated acoustic field, which appears to be "cleaner" when the boundary layer structures are explicitly resolved, with less interference patterns. A possible scenario for this counter-intuitive phenomena may be that the tonal character of the noise source at the lower blade is lowered in this case, thus lowering its interference with the tonal noise source at the upper blade. This scenario will of course require further investigations.

5.3 Other possible strategies: blending approaches

The ZDES mode 3 approach still relies on a transport equation for the turbulence viscosity, meaning that the transport and history of turbulence is accounted for in the model. A different approach relies on a simpler approach in which the switch from RANS to LES is controlled by a simple blending of the turbulence viscosity *i.e.* :

$$\nu_t = (1 - f_P)\, \nu_{t,RANS} + f_P\, \nu_{t,LES} \tag{46}$$

where the RANS eddy viscosity is often obtained by a simple mixing length model, *e.g.* relation (27) and the subgrid viscosity $\nu_{t,LES}$ as a standard LES model. It is worth

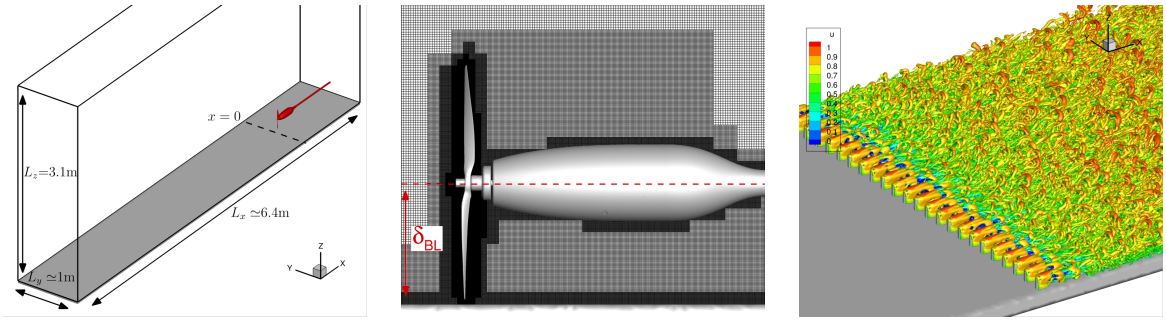


Figure 10: Boundary layer/propeller interaction test case. Left: computational domain; Center: propeller geometry and octree Cartesian grid used; Right: Q criterion iso-surface colored by streamwise velocity near the inflow tripping device.

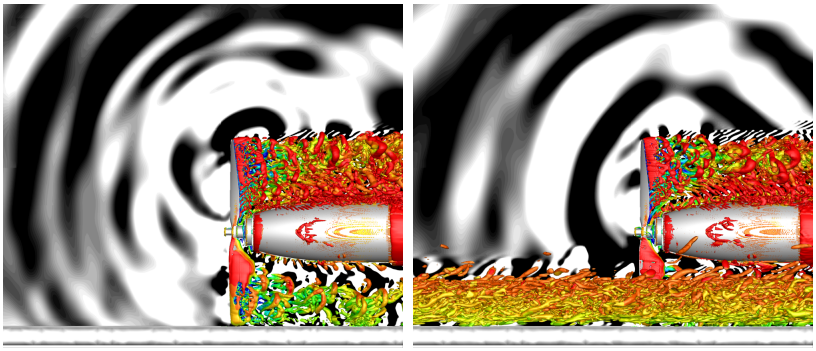


Figure 11: Numerical results from the boundary layer/propeller interaction test case. Instantaneous view of the flow for the ZDES mode 2 (left) and mode 3 (right) simulations. Iso-Q surfaces colored by the streamwise velocity value, gray scale: dilatation field

noting that this blending approach can be easily transposed in the framework of the LBM approach, by considering a hybrid turbulence relaxation time. Although the expressions are not provided in details, the commercial VLES-LBM solver PowerFLOW is based on such a blending, where the blending function is a combination of a local strain, local vorticity and local helicity parameters [47].
A specific WMLES method relying on such a blending is the one proposed by Tamaki and Kawai [55]. In their approach, the linearized SA wall model presented in Section 4.3 is retained in order to minimize the computational effort by using coarser grid resolutions in the wall-normal direction. In an attempt to minimize the log layer mismatch issue[10], the authors model the total shear stress as:

$$\tau_{ij} = 2\rho(\nu + \nu_{t,LES})S^d_{ij} + \tau^{model}_{ij} \tag{47}$$

where S^d denotes the deviatoric part of the rate-of-strain tensor and the modeled turbulent shear stress is expressed as:

$$\tau^{model}_{ij} = \rho u^2_\tau \left(t_i n_j + t_j n_i\right) f_s \tag{48}$$

[10]This is one of the persistent errors in WMLES, where the mean velocity profile in wall units is shifted with respect to the logarithmic law. Although the exact reason for this issue remains unclear, the most plausible explanation is that the increase of eddy viscosity in the near-wall region results in insufficient wall-normal mixing by turbulence in the near-wall region.

where $\mathbf{t}$ and $\mathbf{n}$ are respectively the tangential and wall-normal unit vectors. The blending function f_s between the wall and the RANS-to-LES matching height is expressed as:

$$f_s(y) = \max\left(\frac{y_{match} - y}{y_{match}}, 0\right) \tag{49}$$

In combination with the linearized wall law, relation (47) can be seen as a particular form of (46) where $f_P = f_s$.

6 Summary

In these notes, several RANS/LES methods based on the ZDES approach [18, 17] have been presented and successfully applied to aeroacoustic configurations. In order to further minimize the required computational resources, several wall modeling strategies have also been introduced and coupled with the ZDES. It was shown that the numerical implementation of the wall model may receive particular attention. Indeed, the wall model expression introduces steep velocity gradients near the walls, that may not be properly discretized when coarse or moderate near-wall grid resolutions (typical of wall modeled simulations) are retained. This error has been thoroughly quantified and it results that a significant error may be obtained when evaluating the total shear stress terms near the wall. A possible solution that allows for a control of this error relies on a wall law linearization technique, with specific modeling adaptations, as proposed by Tamaki *et al.*[54]. The use of this linearization method was found very efficient on a wide range of applications and numerical frameworks, *e.g.* in LBM [22]. WMLES strategies where the inner layer of the TBL is modeled in RANS have been shown to yield already interesting results for specific applications that require an explicit resolution of the TBL structures. However, these approaches still represent an open and very active research area, with several specific issues that require to be tackled in more detail. This includes for instance the log layer mismatch or the improvement of turbulent inflow boundary conditions. The development of more advanced wall models is also still a very active research subject, such as with the rise of machine learning strategies *e.g.* [33].

Acknowledgments

The author would like to address special thanks to Julien Husson for providing the ZDES-LBM results on the LEISA2 configuration. Lucas Manueco, Sébastien Deck and Nicolas Renard are also warmly acknowledged for stimulating discussions and interactions.
The author would also like to acknowledge European Union Horizon 2020 research and innovation program under grant agreement no. 860103 (ENODISE), for the funding regarding the development of the ZDES mode 3 approach with wall models and the preparation of this lecture.

References

[1] ProLB: High-fidelity lattice boltzmann CFD simulations. http://www.prolb-cfd.com/.

[2] Turbulence modeling resource. https://turbmodels.larc.nasa.gov/.

[3] N. Afzal. Wake layer in a turbulent boundary layer with pressure gradient: a new approach. *Fluid Mechanics and Its Applications*, 37:95–118, 1996.

[4] S. R. Allmaras, F. T. Johnson, and P. R. Spalart. Modifications and clarifications for the implementation of the Spalart-Allmaras turbulence model. In *Seventh international conference on computational fluid dynamics (ICCFD7)*, pages 1–11. Big Island, HI, 2012.

[5] M. J. Berger and M. J. Aftosmis. An ODE-based wall model for turbulent flow simulations. *AIAA Journal*, pages 1–15, 2017.

[6] W. Cabot and P. Moin. Approximate wall boundary conditions in the large-eddy simulation of high reynolds number flow. *Flow, Turbulence and Combustion*, 63:269–291, 2000.

[7] S-G. Cai, J. Degrigny, J-F. Boussuge, and P. Sagaut. Coupling of turbulence wall models and immersed boundaries on cartesian grids. *Journal of Computational Physics*, 429:109995, March 2021.

[8] F. Capizzano. Turbulent wall model for immersed boundary methods. *AIAA journal*, 49(11):2367–2381, 2011.

[9] F. Capizzano. Automatic generation of locally refined cartesian meshes: Data management and algorithms. *International Journal for Numerical Methods in Engineering*, 113(5):789–813, 2018.

[10] Leandro A. Castelucci, Cornelis H. Venner, and Leandro D. de Santana. *Experimental analysis of the noise of small propellers subjected to non-uniform inflow.*

[11] M. Catchirayer, J.-F. Boussuge, P. Sagaut, M. Montagnac, D. Papadogiannis, and X. Garnaud. Extended integral wall-model for large-eddy simulations of compressible wall-bounded turbulent flows. *Physics of Fluids*, 30(6):065106, 06 2018.

[12] Dean R Chapman. Computational aerodynamics development and outlook. *AIAA journal*, 17(12):1293–1313, 1979.

[13] Nicolas Chauvet, Sebastien Deck, and Laurent Jacquin. Zonal detached eddy simulation of a controlled propulsive jet. *AIAA journal*, 45(10):2458–2473, 2007.

[14] Haecheon Choi and Parviz Moin. Grid-point requirements for large eddy simulation: Chapman's estimates revisited. *Physics of fluids*, 24(1), 2012.

[15] M. Choudhari and M.R. Khorrami. Effect of three-dimensional shear-layer structures on slat cove unsteadiness. *AIAA Journal*, 45:2174–2186, 2007.

[16] T. J. Craft, S. E. Gant, Iacovides, H., and B. E. Launder. A new wall function strategy for complex turbulent flows. *Numerical Heat Transfer, Part B: Fundamentals*, 45(4):301–318, 2004.

[17] S. Deck. Recent improvements in the zonal detached eddy simulation (ZDES) formulation. *Theoretical and Computational Fluid Dynamics*, 26(6):523–550, 2012.

[18] S. Deck and N. Renard. Towards an enhanced protection of attached boundary layers in hybrid RANS/LES methods. *Journal of Computational Physics*, 400:108970, 2020.

[19] S. Deck, P-E. Weiss, and N. Renard. A rapid and low noise switch from RANS to WMLES on curvilinear grids with compressible flow solvers. *Journal of Computational Physics*, 363:231–255, 2018.

[20] Sébastien Deck, Nicolas Renard, Romain Laraufie, and Pierre Sagaut. Zonal detached eddy simulation (ZDES) of a spatially developing flat plate turbulent boundary layer over the reynolds number range $3150 \leq Re_\theta \leq 14000$. *Physics of Fluids*, 26(2), 2014.

[21] J. Degrigny, S-G. Cai, J-F. Boussuge, and P. Sagaut. Improved wall model treatment for aerodynamic flows in LBM. *Computers & Fluids*, 227:105041, September 2021.

[22] J Husson, M Terracol, and S Deck. A critical assessment of navier–stokes and lattice boltzmann frameworks applied to high-lift configuration through a multiresolution approach. *Physics of Fluids*, 36(8), 2024.

[23] J. Husson, M. Terracol, S. Deck, and T. Le Garrec. Critical assessment of wall model numerical implementation in LBM. *Computers & Fluids*, 257:105857, May 2023.

[24] J. Husson, M. Terracol, S. Deck, and T. Le Garrec. A comprehensive framework for robust hybrid RANS/LES simulations of wall-bounded flows in LBM. *Journal of Computational Physics*, 502:112814, April 2024.

[25] Nicolas Jarrin, Sofiane Benhamadouche, Dominique Laurence, and Robert Prosser. A synthetic-eddy-method for generating inflow conditions for large-eddy simulations. *International Journal of Heat and Fluid Flow*, 27(4):585–593, 2006.

[26] L. N. Jenkins, M. R. Khorrami, Choudhari, M. M., and C. B. McGinley. Characterization of unsteady flow structures around tandem cylinders for component interaction studies in airframe noise. AIAA Paper 2005-2812, 2005.

[27] L. N. Jenkins, D. H. Neuhart, C. B. McGinley, M. M. Choudhari, and M. R. Khorrami. Measurements of unsteady wake interference between tandem cylinders. AIAA Paper 2006-3202, 2006.

[28] S. Kawai and K. Asada. Wall-modeled large-eddy simulation of high reynolds number flow around an airfoil near stall condition. *Computers & Fluids*, 85:105–113, 2013. International Workshop on Future of CFD and Aerospace Sciences.

[29] S. Kawai and J. Larsson. Wall-modeling in large eddy simulation: Length scales, grid resolution, and accuracy. *Physics of Fluids*, 24(1):015105, 01 2012.

[30] R. Laraufie, S. Deck, and P. Sagaut. A dynamic forcing method for unsteady turbulent inflow conditions. *Journal of Computational Physics*, 230(23):8647–8663, 2011.

[31] D.P. Lockard. Summary of the tandem cylinder solutions from the benchmark problems for airframe noise computations-I workshop. AIAA Paper 2011-353, 2011.

[32] D.P. Lockard and M. Choudhari. Noise radiation from a leading-edge slat. AIAA Paper 2009-3101, 15th AIAA/CEAS Aeroacoustics Conference, Miami, FL, USA, 11-13 May, 2009.

[33] Adrián Lozano-Durán and H Jane Bae. Machine learning building-block-flow wall model for large-eddy simulation. *Journal of Fluid Mechanics*, 963:A35, 2023.

[34] T. S. Lund, X. Wu, and K. D. Squires. Generation of turbulent inflow data for spatially-developing boundary layer simulations. *J. Comput. Phys.*, 140:233–258, 1998.

[35] H. Maeyama, T. Imamura, J. Osaka, and N. Kurimoto. Unsteady aerodynamic simulations by the lattice Boltzmann method with near-wall modeling on hierarchical cartesian grids. *Computers & Fluids*, 233:105249, January 2022.

[36] E. Manoha and M. Pott-Pollenske. LEISA2: an experimental database for the validation of numerical predictions of slat unsteady flow and noise. AIAA Paper 2015-3137, 21st AIAA/CEAS Aeroacoustics Conference, 2015.

[37] L. Manueco, P-E. Weiss, and S. Deck. On the coupling of wall-model immersed boundary conditions and curvilinear body-fitted grids for the simulation of complex geometries. *Computers & Fluids*, 226:104996, 2021.

[38] F.R. Menter, M. Kuntz, and R. Bender. A Scale-Adaptive Simulation Model for Turbulent Flow Predictions. *AIAA Paper 03-0767, 41th AIAA Aerospace Sciences Meeting and Exhibit, Reno, Nevada*, 2003.

[39] J Mohd-Yusof. For simulations of flow in complex geometries. *Annual research briefs*, 317:35, 1997.

[40] A. J. Musker. Explicit expression for the smooth wall velocity distribution in a turbulent boundary layer. *AIAA Journal*, 17:655–657, 1979.

[41] D. H. Neuhart, L. N. Jenkins, M. M. Choudhari, and M. R. Khorrami. Measurements of the flowfield interaction between tandem cylinders. AIAA Paper 2009-3275, 2009.

[42] Mathieu Pamiès, Pierre-Elie Weiss, Eric Garnier, Sébastien Deck, and Pierre Sagaut. Generation of synthetic turbulent inflow data for large eddy simulation of spatially evolving wall-bounded flows. *Physics of fluids*, 21(4), 2009.

[43] Hans Reichardt. Vollständige darstellung der turbulenten geschwindigkeitsverteilung in glatten leitungen. *ZAMM-Journal of Applied Mathematics and Mechanics/Zeitschrift für Angewandte Mathematik und Mechanik*, 31(7):208–219, 1951.

[44] Nicolas Renard and Sébastien Deck. Improvements in zonal detached eddy simulation for wall modeled large eddy simulation. *AIAA Journal*, 53(11):3499–3504, November 2015.

[45] WC Reynolds. The potential and limitations of direct and large eddy simulations. *Whither Turbulence? Turbulence at the Crossroads*, 357:313–343, 1990.

[46] Pierre Sagaut, Marc Terracol, and Sebastien Deck. *Multiscale and multiresolution approaches in turbulence-LES, DES and Hybrid RANS/LES Methods: Applications and Guidelines*. World Scientific, 2013.

[47] Rajani Satti, Yanbing Li, Richard Shock, and Swen Noelting. Unsteady flow predictions around tandem cylinders with sub-critical spacing. In *49th AIAA Aerospace Sciences Meeting Including the New Horizons Forum and Aerospace Exposition*, page 54, 2011.

[48] Hermann Schlichting and Joseph Kestin. *Boundary layer theory*, volume 121. Springer, 1961.

[49] Philippe R Spalart. Comments on the feasibility of les for wings and on the hybrid rans/les approach. In *Proceedings of the First AFOSR International Conference on DNS/LES, 1997*, pages 137–147, 1997.

[50] Philippe R Spalart, Shur Deck, Michael L Shur, Kyle D Squires, M Kh Strelets, and Andrei Travin. A new version of detached-eddy simulation, resistant to ambiguous grid densities. *Theoretical and computational fluid dynamics*, 20:181–195, 2006.

[51] P.R. Spalart and S.R. Allmaras. A one-equation turbulence model for aerodynamic flows. In *30th Aerospace Sciences Meeting and Exhibit*. American Institute of Aeronautics and Astronautics, 1992.

[52] D. B. Spalding. A single formula for the law of the wall. *Journal of Applied mechanics*, 28(3):455–458, 1961.

[53] M Strelets. Detached eddy simulation of massively separated flows. In *39th Aerospace sciences meeting and exhibit*, page 879, 2001.

[54] Y. Tamaki, M. Harada, and T. Imamura. Near-wall modification of Spalart–Allmaras turbulence model for immersed boundary method. *AIAA Journal*, 55(9):3027–3039, sep 2017.

[55] Yoshiharu Tamaki and Soshi Kawai. Wall modeling for large-eddy simulation on non-body-conforming cartesian grids. *Physical Review Fluids*, 6(11):114603, 2021.

[56] M. Terracol and Manueco L. A dynamic linearized wall model for turbulent flow simulation: towards grid convergence in wall-modeled simulations. *Submitted to Journal of Computational Physics (revised version sent)*, 2024.

[57] M. Terracol and E. Manoha. Wall-resolved large-eddy simulation of a three-element high-lift airfoil. *AIAA Journal*, 58(2):517âĂŞ536, February 2020.

[58] M. Terracol and E. Manoha. Numerical wire mesh model for the simulation of noise-reduction devices. *AIAA Journal*, 59(3):987–1007, mar 2021.

[59] M. Terracol, E. Manoha, and B. Lemoine. Investigation of the unsteady flow and noise generation in a slat cove. *AIAA Journal*, 54(2):469–489, 2015.

[60] M. Terracol, E. Manoha, L. Manueco, F. Avallone, D. Ragni, and A. Rubio Carpo. Numerical simulations of a landing gear with flow through fairings for noise mitigation. In *AIAA Aviation 2023 Forum*, 2023.

[61] Jaime Vaquero, Nicolas Renard, and Sébastien Deck. Advanced simulations of turbulent boundary layers under pressure-gradient conditions. *Physics of Fluids*, 31(11), November 2019.

[62] Jaime Vaquero, Nicolas Renard, and Sébastien Deck. Outer layer turbulence dynamics in a high-reynolds-number boundary layer up to recovering from mild separation. *Journal of Fluid Mechanics*, 942, May 2022.

[63] Jaime Vaquero, Nicolas Renard, and Sébastien Deck. ZDES simulation and spectral analysis of a high-reynolds-number out-of-equilibrium turbulent boundary layer. *Flow, Turbulence and Combustion*, 109(4):1059–1079, August 2022.

[64] Wang M. and Moin P. Dynamic wall modeling for large-eddy simulation of complex turbulent flows. *Physics of Fluids*, 14(7):2043–2051, 2002.

[65] S. Wilhelm, J. Jacob, and P. Sagaut. An explicit power-law-based wall model for lattice boltzmann methodâĂŞreynolds-averaged numerical simulations of the flow around airfoils. *Physics of Fluids*, 30(6), June 2018.

[66] X. I. A. Yang, J. Sadique, R. Mittal, and C. Meneveau. Integral wall model for large eddy simulations of wall-bounded turbulent flows. *Physics of Fluids*, 27(2), February 2015.

[67] Xiang IA Yang and Kevin P Griffin. Grid-point and time-step requirements for direct numerical simulation and large-eddy simulation. *Physics of Fluids*, 33(1), 2021.